



Experimental Study of Dynamic Mechanical Response and Energy Dissipation of Rock Having a Circular Opening Under Impact Loading

Hao Wu¹ · Bing Dai^{2,3} · Li Cheng³ · Rong Lu³ · Guoyan Zhao⁴ · Weizhang Liang⁴

Received: 30 May 2020 / Accepted: 12 January 2021 / Published online: 18 February 2021
© Society for Mining, Metallurgy & Exploration Inc. 2021

Abstract

Affected by the disturbance of blasting activities, deformation instability and rock dynamic disasters are prone to occur in deep hard rock roadways. Thus, it is particularly necessary to understand the failure behavior of rocks and roadways under dynamic loads. In this study, a series of impact loading tests were carried out on sandstone samples with and without a circular cavity by a modified split Hopkinson pressure bar (SHPB) test system. The mechanical properties and energy evolution of the samples were systematically investigated, and the effect of cavity size was analyzed. The results showed that the presence of the cavity in the samples weakens the dynamic compressive strength by more than 10%, and the peak strain and brittleness are also reduced to varying degrees. Under dynamic loading, spalling cracks occur first on the roof and floor of the cavity, and then different numbers of shear cracks are formed on the sample diagonals. The eventual shear failure mode is the result of the connection of the shear cracks and the cavity. As the cavity radius increases, the dissipated energy density and fractal dimension both grow accordingly, leading to smaller and smaller rock fragments. The dynamic failure behavior of the circular cavity can be well explained based on the dynamic stress distribution law. Overall, this study can provide a reference for the study of the mechanism of rock burst in deep roadways.

Keywords Blasting · Dynamic fracture behavior · Energy dissipation · Rock containing a cavity · Spalling · Rock fragmentation

1 Introduction

Influenced by early diagenesis or late geological processes, various discontinuities are extensively distributed in natural rocks, e.g., joint, bedding, fault, fissure, pore, and cave. Since stress concentration easily occurs near the corners of these flaws, new cracks usually emanate from these places first, and then propagate in a certain direction until they intersect each other to form a macroscopic failure. In other words,

the failure of rock is generally progressive, which is different from the instantaneous failure of glass material. This makes it possible to warn of rock instability and rock disasters. Also, provided that the rock mass is excavated by drilling and blasting method, the internal flaws are conducive to reducing the consumption of explosives and improving rock fragmentation. On the other hand, the existing flaws make the mechanical properties of rocks greatly weakened and complicate the failure behavior. A couple of reasons can account for these behaviors: (1) The internal structure of the rock is seriously deteriorated by the flaws, which brings about a pronounced degradation in rock strength and stiffness; (2) under the action of external force, micro-cracks tend to appear around the perimeters of the flaws because of high concentrated stress, resulting in further weakening of rock mechanical properties [1–4]; and (3) the number of flaws is unclear and their spatial distribution is random.

According to the shape of flaws, we can classify them into two kinds: crack-type flaw and cavity-type flaw. To find out how pre-existing cracks affect the strength, deformation, and failure features of rocks, a multitude of studies have been performed on jointed rock or rock-like samples under different load conditions in recent years. For prismatic samples

✉ Bing Dai
daibingusc@usc.edu.cn

✉ Weizhang Liang
wzliang@csu.edu.cn

¹ School of Mines, China University of Mining and Technology, Xuzhou 221116, Jiangsu, China

² School of Resource Environment and Safety Engineering, University of South China, Hengyang 421000, Hunan, China

³ Deep Mining Laboratory of Shandong Gold Group Co., Ltd., Laizhou 261400, Shandong, China

⁴ School of Resources and Safety Engineering, Central South University, Changsha 410083, Hunan, China

embedded with a single joint in uniaxial loading, two typical sorts of cracks have been widely identified, namely, wing crack (also known as primary-tensile crack) and secondary crack [5, 6]. The wing crack initiating from the joint tip propagates crookedly in a stable manner as the imposed load increases, and finally remains consistent with the loading direction. The secondary crack whose propagation direction is largely related to rock material generally occurs later than the wing crack, and plays a leading role in the eventual failure. Additionally, several other types of cracks such as anti-wing crack, shear crack, and far-field crack are sometimes found in the uniaxial compression tests, which depend on the length and inclination of the pre-fabricated joint in the sample [7]. Under biaxial and triaxial loading, the confining pressure and joint angle are found to be the prominent factors influencing the failure mode [8–10]. Moreover, the failure characteristics of samples with one joint under other loading methods, e.g., tensile loading, cyclic loading, impact loading, and static-dynamic coupled loading, have also been surveyed and discussed [11–15], which plays a positive role in understanding the mechanism of rock mass instability.

Apart from one crack, considerable research has focused on the situations of two, three, and multiple pre-fabricated joints in gypsum, PMMA, cement mortar, and rock samples as well [16–21]. Results manifested that the sample strength and cracking response are corporately impacted by the number, dimension and configuration of joints, material properties, loading forms, and filling conditions. The failure is an evolutionary process of initiation and propagation of various cracks and different types of joint coalescence. Occurrence of diverse coalescence patterns is a result of competition between a few mechanisms in forming tensile or shear cracks [22]. Moreover, some researchers, e.g., Dyskin et al. [23], Zhang et al. [24], Mondal et al. [25], and Zhou et al. [26, 27] have further explored the crack evolution in samples with 3D-joints under compressive loads, and observed three common classes of cracks growing from the joint tips; that is, wing crack, anti-wing crack, and far-field crack.

Likewise, the cavities ranging from tiny pores to large caves are also widespread in the rock mass, and it is widely shared that the rock having cavities has a higher potential for instability than the intact rock. Besides, in engineering practice, rock burst or V-notched failure often happens at sidewalls or roof of deep-buried hard rock tunnel. Essentially, the tunnel, roadway, and shaft excavated in deep-buried rock mass can be simplified as an artificial cavity in rock sample. Therefore, studying the effect of cavity on mechanical performance and failure features of holey rock is beneficial to control rock stability and reveal tunnel failure mechanism. For this purpose, growing attention has been paid to the cracking behavior of rock or rock-like samples having cavity-type flaws under various loading conditions. For sample having a single cavity

under uniaxial compression, Hoek [28] first discovered three categories of cracks (primary-tensile fracture on roof-floor, spalling fracture on sidewalls, and remote fracture on corners) formed around a circular cavity in photo elastic tests. Wong et al. [29] found that the primary-tensile crack is inclined to initiate and propagate in sample with a small width and a large diameter cavity, which is fairly agreeable with the theoretical results by Sammis-Ashby model [30]. Zhao et al. [31] applied acoustic emission (AE) technique to investigate the fracture evolution around circular cavities, and argued that the peak strength and crack initiation stress mainly rely on the cavity size. Carter et al. [32] measured the initiation stress of the tensile cracks by attaching a number of strain gauges close to the circular cavity. However, the applicability of this method is limited because the propagation paths of the cracks are uncertain. Besides, Zeng et al. [33] experimentally investigated the influence of cavity shape on strength, deformation, and fracturing behavior, and explained the initiation locations of cracks based on the force fields obtained by PFC modeling. To deeply reveal the fracturing mechanisms of different shaped cavities, Wu et al. [34] analytically derived the stress distributions around the cavities using complex variable approach, and reproduced the real-time crack development combining AE and DIC techniques. If the biaxial load is applied, tensile cracks squeezed by lateral pressure no longer appear, and the spalling failure on the cavity sides is more severe [32, 35]. For the case of triaxial compression, the crack initiation stress is larger than that of the biaxial and uniaxial loading, and the failure mode is prominently controlled by the orientation and amplitude of the intermediate principal stress [36]. In regard to the Brazilian disc sample with a central circular cavity under splitting tension, the failure is induced by the coalescence of the primary crack along the loading diameter and the secondary crack parallel with the horizontal diameter [37]. Besides, the failure processes of samples having two or multiple cavities of circular, elliptical, inverted *U*-shaped, and rectangular cavities under different forms of static loads were reported experimentally and numerically [38–46]. Furthermore, to be close to the actual situation of natural rocks, many factors like rock heterogeneity, porosity, and ambient temperature were considered [47–49], which promotes the development of rock mechanics.

From the above review, it can be seen that most studies were conducted under static loads. In practice, openings in hard rock mass are mostly excavated by using drilling and blasting method; that is, the rock mass and opening are subjected to strong dynamic loads caused by mechanical drilling and explosive blasting [50, 51]. Additionally, literature indicates that many rock disasters, especially rock bursts, are caused by dynamic load disturbances [52–55,]. Thus, carrying out investigations on cracking behavior of samples containing a cavity under dynamic loads is helpful to grasp the

deformation and failure mechanism of rock tunnel. In this work, several groups of prismatic sandstone samples with a circular cavity of different diameters were prepared for impact tests by a modified split Hopkinson pressure bar (SHPB) test system. The dynamic failure processes of these samples were monitored by a high-speed camera. Further on, the energy changes during rock failure and fragmentation feature were also analyzed and discussed.

2 Material and Experimental Method

2.1 Sample Preparation

Considering that sedimentary rocks are widely distributed in the Earth's crust, we chose representative brown sandstone with medium strength as the test material in this work. This sort of rock originating from a quarry in Linyi City in eastern China was transported to a professional geotechnical company in Liuyang City for processing. The results of optical microscopy analysis show that the rock has good homogeneity and integrity, and the main mineral components are SiO_2 (46%), $\text{Na}[\text{AlSi}_3\text{O}_8]\text{-Ca}[\text{Al}_2\text{Si}_2\text{O}_8]$ (35%), CaCO_3 (9%), $\text{A}_m\text{B}_p\text{O}_{2p}\cdot n\text{H}_2\text{O}$ (8%), $\text{K}[\text{AlSi}_3\text{O}_8]$ (5%), and 1% other transparent substances (see Fig. 1) [56]. Additionally, the rock owns a massive structure, and its particle size varies from 0.15 to 0.50 mm, which belongs to the medium-fine grade.

In this research, we prepared a total of four groups of samples: group D-1, group D-2, group D-3, and group D-4. Each group contains three identical samples. The samples of group D-1, namely, D-1-A, D-1-B, and D-1-C (A/B/C represents the sample number in the same group) are intact and used for comparison with other groups. Group D-2 are samples containing a circular cavity with a radius of 3 mm, while the radius of the hole inside the samples of group 3 and group 4 are 4 mm and 5 mm. All the samples were separated from a

complete sandstone block and machined into prisms with sizes of $45 \times 45 \times 20$ mm (length \times width \times thickness) via a rock cutter, as illustrated in Fig. 2. The size design is mainly based on the following reasons: (1) The cross-sectional areas of the loading ends of the sample shall be smaller than those of the bars; (2) the length-width ratio of the sample should meet 1:1, and the length and width of the sample should be large enough to eliminate the boundary effect caused by cavity excavation; and (3) the sample should be thin enough to ensure that the surface cracking and internal fracture are consistent. As the hydraulic cutting method causes less damage to the rock than the mechanical cutting method, the high-pressure water jet technique was adopted to excavate the central circular cavities in the samples. Besides, the six surfaces of each specimen need to be polished so that the unevenness does not exceed 0.02 mm, and the non-perpendicularity between parallel surfaces is less than 0.001 radian.

Before the start of the impact test, several conventional physico-mechanical property indexes of this rock were measured firstly in accordance with the relevant experimental specifications, as shown in Table 1.

2.2 Testing Equipment and Principle

A set of modified SHPB test equipment [57] in the rock dynamics laboratory of Central South University was used to carry out impact tests on these samples, which is presented in Fig. 3. It consists of three parts: impact loading system, signal acquisition system, and image acquisition system.

The impact loading system is comprised of a nitrogen container, an excitation device, a self-designed spindle-shaped striker, an incident bar, a transmission bar, a buffer bar, and a pedestal. Compared with the conventional loading method of rectangular waves generated by a cylindrical striker, the loading method of half-sine wave induced by the spindle-shaped striker can solve the problems of wave dispersion,

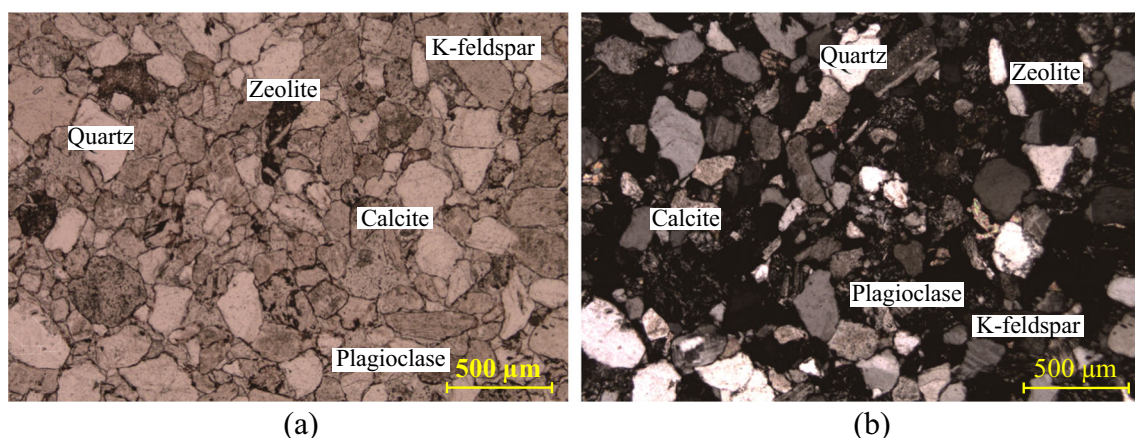


Fig. 1 Photos of mineral compositions in brown sandstone slice by polarizing microscope: **a** under single polarized light; **b** under orthogonal polarized light (quartz— SiO_2 ; plagioclase— $\text{Na}[\text{AlSi}_3\text{O}_8]\text{-Ca}[\text{Al}_2\text{Si}_2\text{O}_8]$; calcite— CaCO_3 ; zeolite— $\text{A}_m\text{B}_p\text{O}_{2p}\cdot n\text{H}_2\text{O}$; K-feldspar— $\text{K}[\text{AlSi}_3\text{O}_8]$).

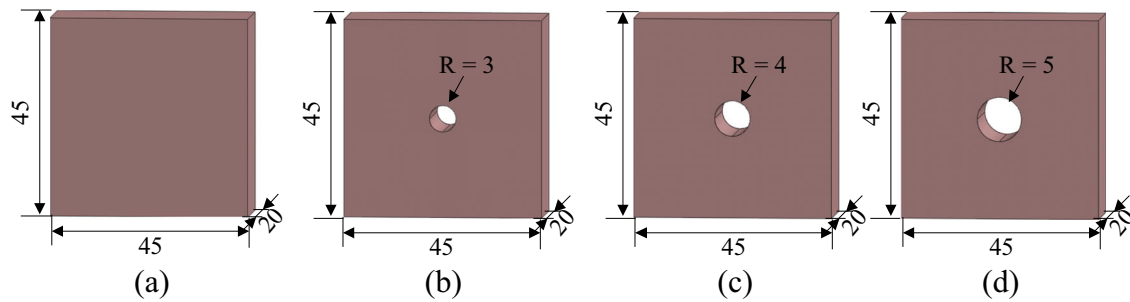


Fig. 2 Diagram of four groups of processed samples for SHPB test: **a** sample D-1; **b** sample D-2; **c** sample D-3; **d** sample D-4

large change of strain rate, repeated loading, and unloading during rock impact loading, which is particularly suitable for rock dynamic performance testing [58]. The striker and bars are both made of 40Cr alloy steel with an elastic modulus of 233 GPa and a density of 7821 kg/m^3 . The diameters of the incident, transmission, and buffer bars are all 50 mm, and the lengths are 2.0 m, 1.5 m, and 0.5 m, respectively. The average wave speed of these bars is measured as 5461 m/s.

With respect to the signal acquisition system, it is made up of two strain gauges (B120-2AA), two bridge boxes, a dynamic strain meter and an oscilloscope. The oscilloscope with model of DL-850E is produced by Yokogawa, Japan. It has a data update rate of 1 MHz (1 μs), a minimum measurement resolution of 625 ps, and a measurement range (frequency) of 0.01 Hz to 500 kHz. The model of the dynamic strain meter purchased from Beidaihe practical electronic technology research institute is SDY2107A. The frequency band of the dynamic strain gauge is 0~1 MHz, and the applicable range of the bridge resistance is 60~1000 Ω . It has automatic balancing and calibration functions, and the quarter-bridge strain gauge measuring mode is adopted. Besides, a laser velocimeter was placed near the end of excitation device to monitor the impact speed of the striker.

For the image acquisition system, it is composed of a high-speed camera and a light source. The high-speed camera used for recording the failure process of sample is produced by Photron company, with a model of Fastcam Sa1.1. Its chip is a 12-bit CMOS sensor with a maximum shooting speed of 675,000 FPS. To clearly capture the photos of the sample during the tests, a high-power fill light is usually arranged next to the high-speed camera. The acquisition rate of the camera is designed to be 75,000 FPS, namely, one photo is taken every 13.33 μs . Note that the camera starts to work when the strain gauge on the

incident bar is first triggered by the stress wave, so the loading time of sample t_s can be calculated according to: $t_s = t - t_0$, where t is the oscilloscope running time and t_0 is the time that the stress wave propagates from the strain gauge to the interface between the incident bar and the specimen minus the signal processing time. Literature shows that t_0 is 147.20 μs [58]. That is, the twelfth picture taken by the camera in this study is the initial moment of sample deformation under loading.

Figure 4 shows the propagation process of the stress wave in the impact loading system. When the excitation device is started, a certain pressure of nitrogen from the nitrogen tank will drive the striker to hit the incident bar, leading to the formation of incident stress wave. The amplitude of the stress wave is positively related to the nitrogen pressure, and this system has a maximum impact load of 500 MPa. In this work, the impact pressure for each test is set to 0.45 MPa. The stress wave first propagates at a constant speed along the incident bar, and then transmits and reflects at the interface I between the incident bar and the sample. After that, the stress wave propagates steadily in the sample, and transmits and reflects again at the interface II between the sample and the transmission bar. The signals of the first incident and reflected waves can be picked up by the strain gauge 1, while those of the transmitted wave appeared firstly in the transmission bar can be monitored by the strain gauge 2. Since the length of the sample is very small, the time for the stress wave to go back and forth in the rock sample is very short. After several times of transmissions and reflections, the stress and strain in the rock sample are basically the same. That is to say, the stress uniformity hypothesis can be satisfied.

According to the one-dimensional stress wave theory [58–60], the displacement $u(t)$ of particle can be written as follows:

Table 1 Main physico-mechanical property indexes of brown sandstone sample

Density, ρ	2472.2 kg/m^3	Young's modulus, E	24.4 GPa
P wave velocity, v	3174.5 m/s	Poisson's ratio, μ	2.17
Tensile strength, σ_t	5.3 MPa	Angel of internal friction, ϕ	40.4°
Uniaxial compressive strength, σ_c	102.6 MPa	Cohesion, c	19.0 MPa
Crack initiation stress, σ_i	44.8 MPa	Fracture toughness, K_{IC}	0.6 $\text{MPa}\cdot\text{m}^{0.5}$

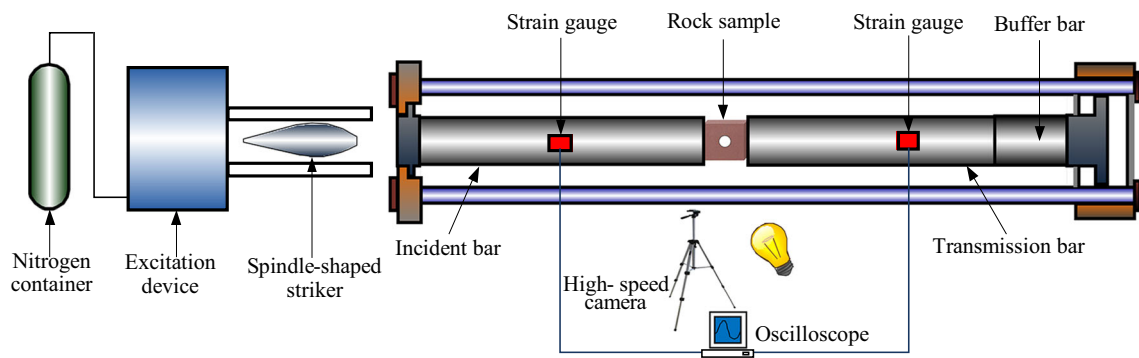


Fig. 3 SHPB equipment for impact loading tests

$$u(t) = C \int_0^t \varepsilon(t) dt \tag{1}$$

where C denotes the wave speed, t means the time, and ε is the strain.

If the incident, reflected and transmitted strains are denoted by $\varepsilon_i(t)$, $\varepsilon_r(t)$ and $\varepsilon_t(t)$, respectively, the displacements (u_1 and u_2) of the interfaces I and II can be expressed as follows:

$$\begin{cases} u_1 = C \int_0^t (\varepsilon_i(t) - \varepsilon_r(t)) dt \\ u_2 = C \int_0^t \varepsilon_t(t) dt \end{cases} \tag{2}$$

Therefore, the average strain ε_s of the sample whose length is represented by l_s can be concluded as follows:

$$\varepsilon_s(t) = \frac{u_1 - u_2}{l_s} = \frac{C}{l_s} \int_0^t (\varepsilon_i(t) - \varepsilon_r(t) - \varepsilon_t(t)) dt \tag{3}$$

Based on the uniformity hypothesis, substituting $\varepsilon_i + \varepsilon_r = \varepsilon_t$ into Eq. (3), we have as follows:

$$\varepsilon_s(t) = -\frac{2C}{l_s} \int_0^t \varepsilon_r(t) dt \tag{4}$$

By differentiating Eq. (4), the strain rate of the sample can be solved, namely

$$\dot{\varepsilon}_s(t) = \frac{2C}{l_s} \varepsilon_r(t) \tag{5}$$

where $\dot{\varepsilon}_s$ represents the strain rate of the sample.

The loads at both ends of the sample can be calculated by the following:

$$F_1 = EA(\varepsilon_i(t) + \varepsilon_r(t)), \quad F_2 = EA\varepsilon_t(t) \tag{6}$$

where F_1 and F_2 are the loads on the left and right ends of the specimen, respectively. A and E means the cross-sectional area and elastic modulus of the bars.

For the average stress in the sample, it can be found according to the following:

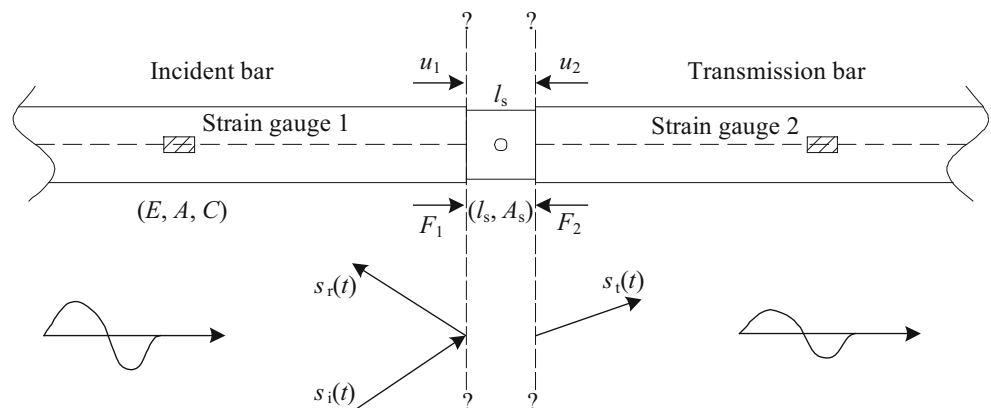
$$\sigma_s = \frac{F_1 + F_2}{2A_s} \tag{7}$$

where σ_s denotes the stress in the sample and A_s represents the cross-sectional area of the sample.

Substituting Eq. (7) into Eq. (6) and combining the stress uniformity hypothesis, we get the following:

$$\sigma_s = E \left(\frac{A}{A_s} \right) \varepsilon_t(t) \tag{8}$$

Fig. 4 Propagation of stress wave in impact loading tests



To conclude, based on the monitored strain signals, the dynamic mechanical parameters ($\varepsilon(t)$, $\dot{\varepsilon}_s(t)$, σ_s) of the samples can be calculated by Eqs. (4), (5), and (8).

3 Experimental Results

3.1 Verification of Stress Uniformity

Firstly, impact tests without placing a sample were carried out to calibrate the SHPB system. When the amplitudes of the incident and transmitted waves in three consecutive tests are basically equal and the reflected wave is close to a straight line, the accuracy of the SHPB system can be deemed to meet the test requirements.

In the present study, the sample D-1-A was taken as an example to verify the stress equilibrium in the sample. Based on the monitored voltage signals of the incident, reflected and transmission waves, the changes of stresses on the two loading surfaces (I and II) of the sample with the loading time can be plotted in Fig. 5a.

As can be seen in Fig. 5a, the curve of stress I agrees well with that of the stress II, especially before the peak point. This suggests that the stress state of the two loading ends of the prismatic sample is the same before failure. Prior to the peak, the sample can be regarded as an elastomer and is macroscopically intact. After the peak stress, damage occurs in the sample and many cracks are formed. Thus, the amplitude of the propagating stress wave will decrease when it encounters cracks. Moreover, Fig. 5b further illustrates the stress states of the loading ends of the sample having a small circular cavity under the same impact load. It is found that the stress at interface II is slightly smaller than that at interface I. The reason is that the stress wave reflects and scatters when it encounters a crack on the propagation path, and then its amplitude is reduced. To sum up, the stress uniformity hypothesis

of the prismatic sample under impact loading using SHPB system can be satisfied, which is consistent with the viewpoint of Li et al [61].

3.2 Dynamic Mechanical Properties of Samples

Table 2 lists the mechanical properties of the four groups of samples subjected to dynamic loading. In each experiment, the speed of the striker is approximately 10 m/s, so the dynamic load applied to each sample is basically the same. According to Table 2, it is calculated that the average dynamic compressive strength (DCS) of the samples from group D-1 to group D-4 is 186.69 MPa, 161.23 MPa, 150.46 MPa, and 145.95 MPa, respectively. Compared with the intact sample, the DCS of the samples with small, medium, and large cavities decreases by 13.64%, 19.40%, and 21.82%, respectively. It is clearly seen that the embedded cavities obviously degrade the DCS of the rock samples, and the degree of weakening is positively related to the cavity size.

The dynamic elastic modulus (DEM) is defined as the slope of the dynamic stress-strain curve where the dynamic stress is half the peak. From Table 2, the average DEM of the four groups of samples (D1~D4) is 26.54 GPa, 25.41 GPa, 25.48 GPa, and 24.36 GPa, respectively. Therefore, it can be summarized that the DEM of the sample is also weakened by the cavity to a certain extent, but the weakening effect is not very significant. Besides, the average peak strains of the four groups of samples are 8.92‰, 8.11‰, 7.38‰, and 7.51‰, respectively. The peak strain of the rock samples having a cavity decreases slightly compared with that of the intact samples, which basically shows a linear relationship with the cavity size. In addition, we found that the strain rate of the sample generally rises with the increase of the cavity radius, with a range of 60 to 80 s⁻¹. It is also shown that the DCS of the samples in the same group increases as the strain rate increases, which is called strain rate effect.

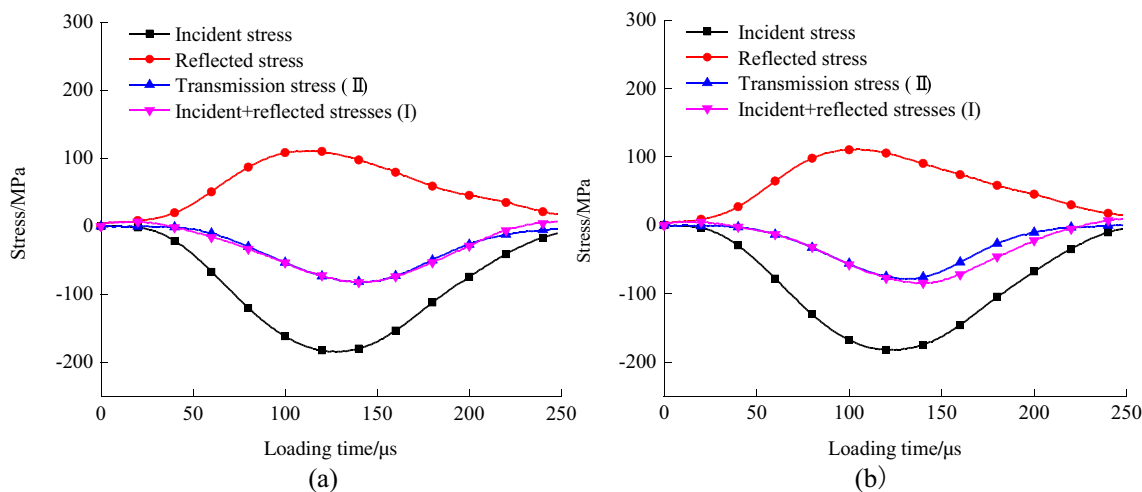


Fig. 5 Curves of different stress waves versus loading time: **a** sample D-1-A; **b** Sample D-2-A

Table 2 Physical-mechanical property parameters of samples under impact loading

Sample no.	Length/mm	Thickness/mm	Width/mm	Density/g·cm ⁻³	Striker speed/m·s ⁻¹	DCS/MPa	DEM/GPa	Peak strain/‰	Strain rate/s ⁻¹
D-1-A	45.7	19.8	45.6	2.44	10.05	180.50	22.99	9.18	64.65
D-1-B	45.0	19.9	44.9	2.45	9.76	194.46	26.03	10.09	74.78
D-1-C	45.1	20.7	45.2	2.47	10.18	185.11	30.60	7.48	50.67
D-2-A	45.5	19.9	45.7	2.43	9.97	169.16	26.22	8.82	68.81
D-2-B	45.1	19.8	45.1	2.43	10.27	157.36	25.44	8.21	79.52
D-2-C	45.2	19.8	45.2	2.45	9.83	157.18	24.58	7.30	66.73
D-3-A	45.8	19.9	45.8	2.41	10.04	158.33	25.48	7.63	69.87
D-3-B	45.1	19.8	45.1	2.43	9.69	146.19	25.78	7.02	64.18
D-3-C	45.1	19.9	45.1	2.43	9.84	146.87	25.17	7.50	63.39
D-4-A	45.8	19.7	45.8	2.42	10.37	161.38	25.20	7.28	76.13
D-4-B	45.6	19.7	44.9	2.42	9.88	143.79	25.14	7.74	76.23
D-4-C	45.8	19.6	45.0	2.44	9.98	132.68	22.74	7.51	81.77

The loading direction is parallel to the length direction of the sample

The representative dynamic stress–strain curves of the four sets of samples under impact loading are presented in Fig. 6. Since the dynamic loading process is quite short, there is no obvious initial pores and micro-cracks compaction stage at the beginning of loading. Only elastic deformation stage, plastic deformation stage, and post-peak deformation stage are formed. The slope of the stress–strain curve of the intact sample in the post-peak stage is very large, suggesting the brittleness of the sample is extremely significant. By contrast, the brittleness of the samples having cavities is not very significant as that of the intact sample. Accordingly, the existence of the cavity enhances the plasticity of the rock sample. Moreover, compared with the samples with a cavity under uniaxial loads [62], no significant stress drops on the stress–

strain curves under dynamic loads is observed. This shows that the dynamic crack development is exceedingly fast.

3.3 Dynamic Fracture Process and Failure Mode

According to the recorded photos of the samples by a high-speed camera during the impact tests, we selected several representative photos for failure analysis. The failure states of the samples at different loading times are shown in Table 3. In the table, the marked cyan notes at the bottom of the sample indicate the dynamic loading time, and the blue notes denote the appeared cracks during the loading. Among the blue notes, the number indicates the crack type (numbers 1, 2, and 3 are defined as tensile cracks, shear cracks, and spalling cracks, respectively), and the superscript letters mean the order in which the cracks form.

As can be seen in Table 3, the failure behavior of these samples under impact loading is clearly displayed. For the intact sample D-1-C, several splitting tensile cracks gradually appear as the loading time T increases. When $T = 2172 \mu\text{s}$, a splitting tensile crack 1^a induced by the axial load is formed at the top of the sample and propagates along the impact direction, and a shear crack 2^a with an angle to the loading direction is also observed at the bottom. When the loading time rises to $2200 \mu\text{s}$, the above two cracks develop further. Meanwhile, the other two tensile cracks (1^b and 1^c) initiate from the two loading ends and propagate horizontally. At $T = 2269 \mu\text{s}$, another tensile crack 1^d is found to grow from the left towards the right loading end. Also, the other non-penetrating shear crack 2^a at the central of the sample surface starts to propagate, which is caused by surface spalling. When T reaches $2408 \mu\text{s}$, it is found that the tensile cracks 1^a~1^c have connected the left and right ends, leading to instability of the sample. Obviously,

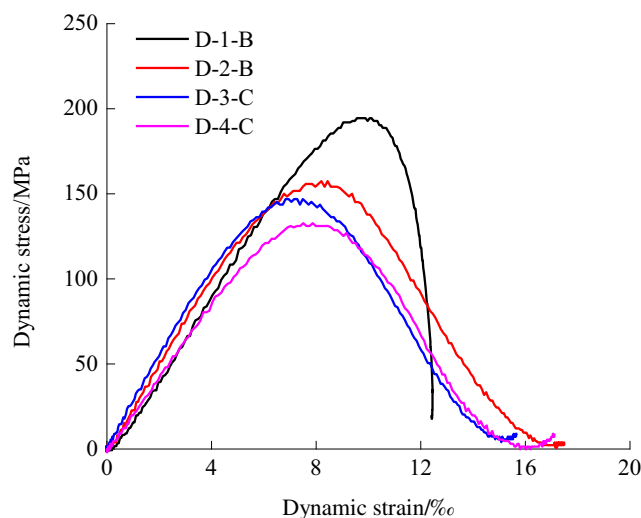


Fig. 6 Dynamic stress–strain curves of representative samples under impact loading

the failure of the intact sample is attributed to the splitting tensile cracks, while the shear cracks that result from the end friction effect do not dominate it. Thus, the failure mode of the intact sample subjected to dynamic loads can be regarded as tensile failure.

With respect to the sample D-2-B, its dynamic failure process is presented in Table 3. When $T = 2013 \mu s$, it can be seen that spalling failure occurs on the roof and floor of the cavity, leading to the appearance of spalling cracks 3^a and 3^b and the ejection of rock slices. With the increase of loading time to $T = 2039 \mu s$, three shear cracks $2^a \sim 2^c$ on the diagonals begin to develop towards the cavity. At $T = 2066 \mu s$, the shear cracks 2^b and 2^c have been connected with the cavity and the shear crack 2^a is about to reach the cavity. Besides, the other two shear cracks 2^c and 2^d are also formed and have merged with the shear crack 2^b . At $T = 2146 \mu s$, the sample loses its integrity due to the intersection of the shear cracks $2^a \sim 2^c$ with the cavity. To summarize, the failure mode of the sample D-2-B is still shear-dominated failure. Table 3 also illustrates the dynamic failure processes of the samples D-3-C and D-4-A, which are similar to that of the sample D-2-B. To put it

differently, the spalling failure occurs first at the top and bottom of the cavity, and then different numbers of shear cracks appear on the diagonals and extend toward the cavity until they are connected. The failure patterns of the two samples under dynamic uniaxial loading also belong to shear-typed failure.

3.4 Energy Dissipation and Rock Fragmentation

According to the energy conservation equation, the calculation formulas of incident energy W_I , reflected energy W_R , transmitted energy W_T , and dissipated energy W_S in the SHPB test system can be derived, namely [59]:

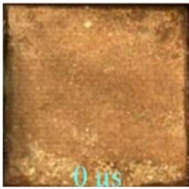

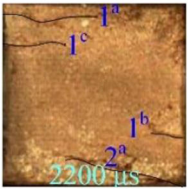
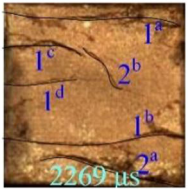
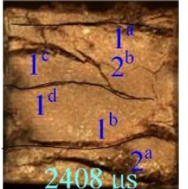
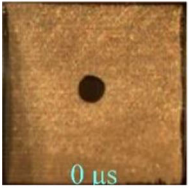
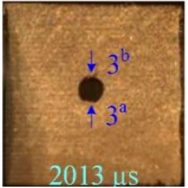
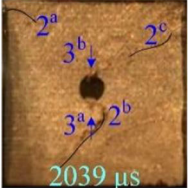
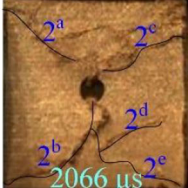
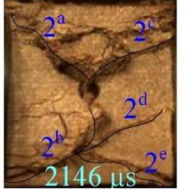
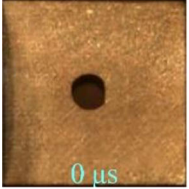
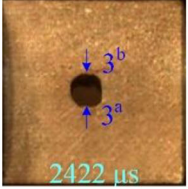
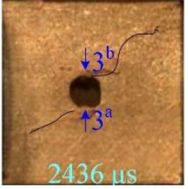
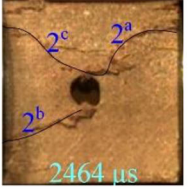
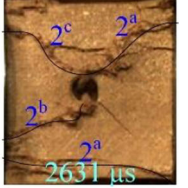
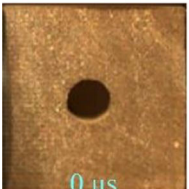
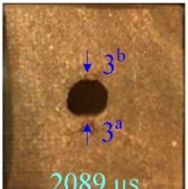
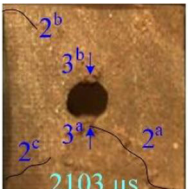
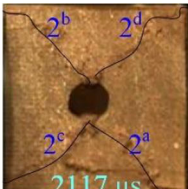

$$W_I = \frac{AC}{E} \int_0^t \sigma_i^2(t) dt \tag{9}$$

$$W_R = \frac{AC}{E} \int_0^t \sigma_r^2(t) dt \tag{10}$$

$$W_T = \frac{AC}{E} \int_0^t \sigma_t^2(t) dt \tag{11}$$

$$W_S = W_I - W_R - W_T \tag{12}$$

Table 3 Failure processes of samples under impact loading

Sample no.	Moment 1	Moment 2	Moment 3	Moment 4	Moment 5
D-1-C					
D-2-B					
D-3-C					
D-4-A					

Since the color of the fill light is yellow, the sample in the photos is also yellow. Besides, the impact direction is horizontal. The crack labels denote the type (the numbers 1, 2 and 3 are defined as tensile cracks, shear cracks and spalling cracks, respectively) of the cracks and their order (a, b, c, d...)

Table 4 Energy characteristic parameters of samples under impact loading

Sample no.	W_I/J	W_R/J	W_T/J	W_S/J	$\rho_W/J\cdot\text{cm}^{-3}$
D-1-A	142.08	52.69	22.57	66.82	1.62
D-1-B	136.65	44.31	28.83	63.51	1.58
D-1-C	140.35	40.89	27.32	72.14	1.71
D-2-A	141.72	53.62	18.03	70.07	1.72
D-2-B	150.02	69.50	14.22	66.31	1.67
D-2-C	133.16	49.25	14.76	69.14	1.73
D-3-A	139.70	50.09	15.16	74.44	1.83
D-3-B	130.45	49.60	12.76	68.09	1.73
D-3-C	135.36	58.10	12.87	64.40	1.63
D-4-A	154.18	62.63	14.57	76.97	1.94
D-4-B	141.41	59.66	11.52	70.23	1.81
D-4-C	145.15	70.08	9.45	65.62	1.69

$$\rho_W = W_S/V_S \tag{13}$$

where σ_i , σ_r , and σ_t represent the incident wave stress, reflected wave stress, and transmitted wave stress, respectively, which can be solved according to Hooke’s law. ρ_W and V_S are the dissipated energy density and the volume of the sample.

Based on the picked strain signals, the detailed values of W_I , W_R , W_T , W_S , and ρ_W of each sample can be achieved according to Eqs. (9)–(13), as shown in Table 4. It is seen that the incident energy range is within 130–150 J at the same pressure, and the reasons for the slight difference are (1) affected by the pressure in the nitrogen tank and manual operation, the amount of nitrogen flowed into the excitation device in each test may be a little

different; (2) the initial position of the manually placed striker cannot be exactly the same. Generally, the energy absorbed during the failure of the specimens is mainly used for crack initiation, propagation, and coalescence. Hence, the rock fragmentation highly depends on the dissipated energy. In this research, the dissipated energy density was employed to characterize the rock fragmentation. The larger the value of this indicator, the more cracks generated inside the sample, that is, the smaller the size of the sample fragment after failure. The average values of the dissipated energy density of the four groups of samples are $1.64\text{ J}\cdot\text{cm}^{-3}$, $1.71\text{ J}\cdot\text{cm}^{-3}$, $1.73\text{ J}\cdot\text{cm}^{-3}$, and $1.81\text{ J}\cdot\text{cm}^{-3}$, respectively. Clearly, the larger the size of the pre-fabricated cavity, the more severe the failure of the specimens.

To further analyze the failure degree of the sample having a cavity under dynamic loading, fractal theory was applied to study the fractal characteristics of rock fragmentation. In this work, a cuboid iron box was placed on the experimental platform to collect rock fragments during the tests. As the front surface of the box needs to be opened for the high-speed camera to take photos, some rock fragments will be ejected from the front opening, but most rock debris can be collected. For the collected sample fragments, a series of standard sieves with mesh diameters of 5, 10, 15, 20, and 40 mm were used to sift them. The cumulative weight of rock fragments at each particle size grade is shown in Table 5.

Literature demonstrates that the distribution of rock fragments can be formulated as [60]:

$$\frac{m_d}{m_t} = \left(\frac{d}{d_m}\right)^{3-D} \tag{14}$$

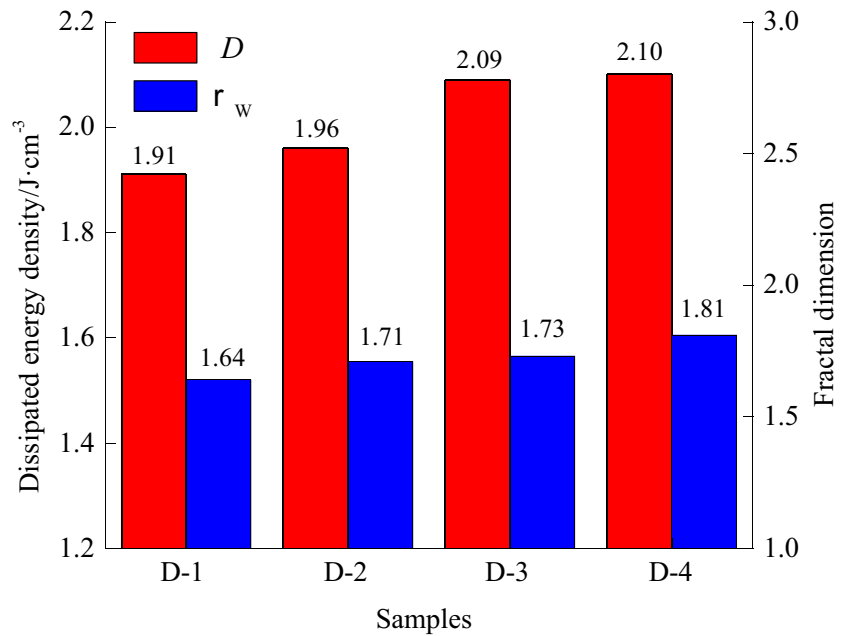
where m_d means the cumulative weight of sample fragments with a particle size smaller than d . m_t denotes the total weight

Table 5 Energy characteristic parameters of samples under impact loading

Sample no.	$m_{d < 5/g}$	$m_{d < 10/g}$	$m_{d < 15/g}$	$m_{d < 20/g}$	$m_{d < 40/g}$	m_t/g	D
D-1-A	12.32	27.82	47.57	58.63	74.90	74.90	2.11
D-1-B	10.13	20.30	36.39	78.30	83.57	83.57	1.89
D-1-C	7.14	16.19	23.33	44.30	93.75	93.75	1.74
D-2-A	9.15	14.69	33.08	45.40	76.91	76.91	1.91
D-2-B	14.25	28.69	55.03	60.72	84.80	84.80	2.11
D-2-C	9.63	20.22	35.6	67.01	88.97	88.97	1.86
D-3-A	14.45	32.84	43.84	61.06	82.72	82.72	2.15
D-3-B	13.67	22.84	44.13	62.65	79.19	79.19	2.09
D-3-C	12.57	23.82	35.45	49.45	88.88	88.88	2.05
D-4-A	17.10	29.21	43.60	61.44	89.67	89.67	2.18
D-4-B	10.78	22.26	36.36	44.82	84.07	84.07	2.01
D-4-C	15.09	25.72	45.45	64.54	84.82	84.82	2.12

$m_{d < 5}$ denotes the weight of the rock fragment whose particle size is below 5 mm. The meanings of $m_{d < 5}$, $m_{d < 10}$, $m_{d < 15}$, $m_{d < 20}$, and $m_{d < 40}$ can be deduced by analogy

Fig. 7 Average fractal dimension and dissipated energy density of different groups of samples under impact loading



of the collected rock fragments. d is the particle size of rock fragments, and d_m is the maximum size of rock fragments (40 mm in this study). D represents the fractal dimension of the sample fragments.

Taking the logarithms on both sides of Eq. (14), it is found that (3-D) is the slope of $\lg(m_d/m_v) - \lg(d/d_m)$ curve. Based on the data in Table 5, the D -value of each sample can be solved via linear fitting, which is listed in Table 5. The average fractal dimensions of the four groups of samples are 1.91, 1.96, 2.09, and 2.20, respectively. Clearly, the fractal dimension of the sample having a cavity is larger than that of the intact sample. The larger the cavity size, the larger the fractal dimension of the sample. Research has shown that the larger the fractal dimension, the more severe the failure of the sample and the smaller the rock fragments [63]. Thus, the rock fragment of the sample having the largest cavity is the smallest, while that of the intact sample is the largest. As illustrated in Fig. 7, both the fractal dimension and the dissipated energy density of the rock sample fragments increase with the growing of the hole radius. This indicates that the existence of hole defects promotes the failure of samples. In summary, the rock fragmentation features of these samples characterized by fractal

dimension index are agreeable with that by dissipated energy density index.

4 Discussion

The crack development in the specimen under load is largely associated with the internal stress state. Generally, tensile cracks are more likely to appear in the tensile stress concentration area, while shear cracks are caused by the high concentrated compressive stress. Therefore, understanding the stress distribution in the sample subjected to different forms of loads is useful to explain the cracking mechanism and failure behavior.

In our previous study, we have conducted uniaxial compression experiments on the prismatic brown sandstone sample with a circular-shaped cavity, and have examined the crack evolution around the cavity via digital image correlation technique [64]. It is observed that four kinds of cracks sequentially appear next to the cavity during the compression process, i.e., primary-tensile cracks ($1^a \sim 1^b$), secondary-tensile cracks ($2^a \sim 2^c$), spalling cracks ($3^a \sim 3^b$), and shear cracks

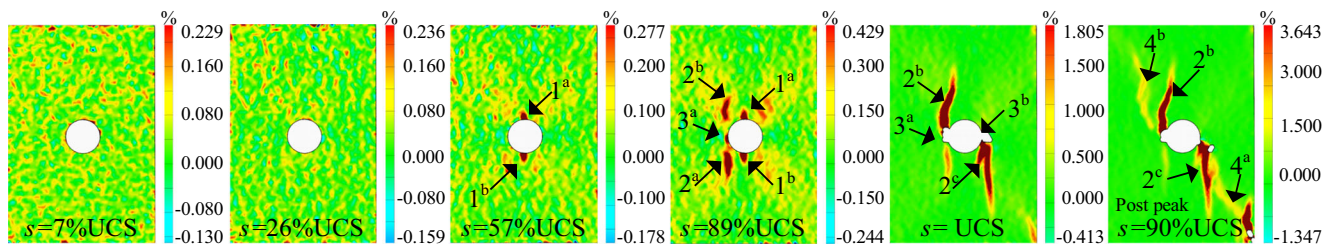


Fig. 8 Distributions of major principal strain of sample with a circular cavity under uniaxial loading

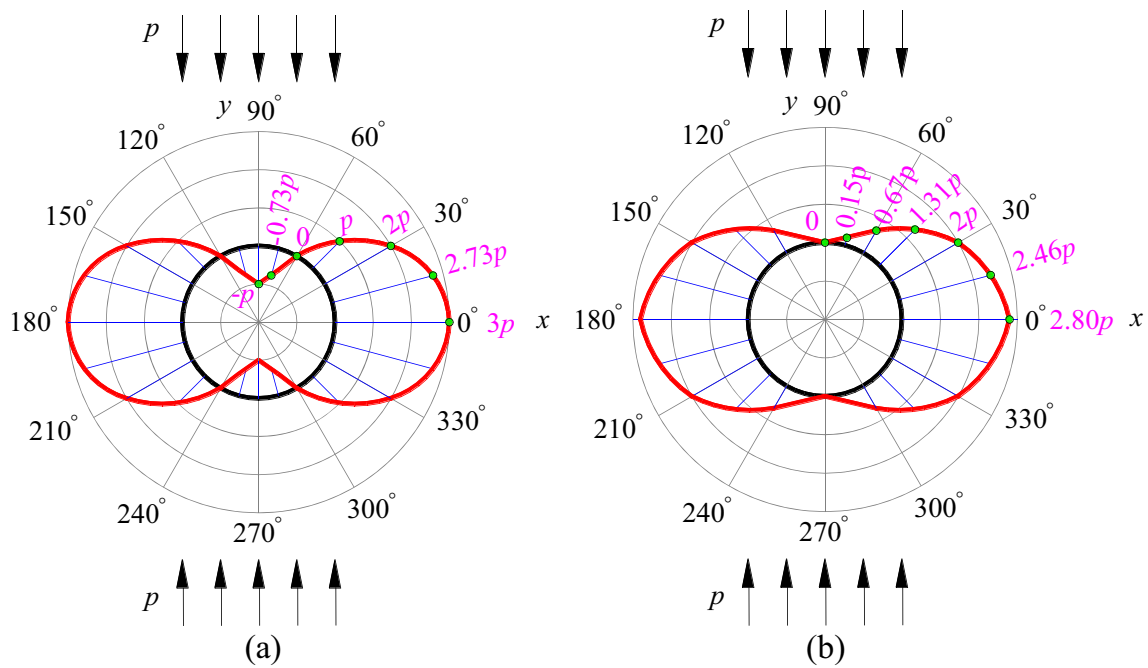


Fig. 9 Hoop stress distributions on the boundary of circular cavity: **a** under uniaxial compressive load; **b** under one-dimensional dynamic load

(4^a–4^b), which is presented in Fig. 8. In this figure, UCS and σ denote the uniaxial compressive strength and axial stress. According to the Kirsch equation, the hoop stress distribution on the boundary of a circular hole only under vertical load p can be plotted in Fig. 9a. Consequently, the primary-tensile cracks first appear in the tensile stress concentration areas (top and bottom of the circular cavity), and propagate along the loading direction. When the cracks reach the edges of the tensile stress areas, the critical stress zones transfer from the tips of the primary-tensile cracks to their either side. It can be calculated that the length of the primary-tensile cracks is $(\sqrt{3} - 1)r_0$ (r_0 denotes the cavity radius). This results in the occurrence of the secondary-tensile cracks, which distribute at the corners of the cavity and also propagate parallel to the loading direction. Owing to the lateral squeeze caused by the secondary-tensile cracks, the primary-tensile cracks close progressively. Actually, the presence of the two types of cracks both results from the concentrated tensile stress. With the gradual increase of the applied load, the concentrated compressive stress ($3p$) on the two sidewalls of the cavity significantly increases, which eventually leads to flaking of the spalling cracks. Moreover, affected by the friction effect at the loading ends of the sample, the shear stress on the diagonal of the sample becomes larger and larger, which will form a shear band and evolve into shear cracks. When they extend to the cavity sidewalls, the specimen loses integrity and fails, resulting in a shear-dominated failure mode.

By contrast, the dynamic stress distribution on the boundary of the circular cavity under one-dimensional impact loads can be obtained using the wave function expansion method, as shown in Fig. 9b. The detailed derivation process can be

found in reference [65]. It is found that the stress distributions around the circular cavity under dynamic and static loads are different. Note that the circular hole is symmetric with respect to the x -axis and y -axis, so only the stresses of the six monitoring points in the figure have been marked, and the stress magnitude of their symmetric points is the same. Since there is no external force applied to the cavity boundary, the radial stress on the perimeter of the hole is zero. For the hoop stress distribution on the cavity boundary, at the position $\theta = 0, r = r_0$, the static and dynamic compressive stress are $3p$ and $2.8p$. At $\theta = \pi/2, r = r_0$, the static and dynamic compressive stress concentration factors are -1 and 0 . Interestingly, no tensile stress is observed on the boundary of the circular cavity subjected to dynamic loads. As a result, no tensile cracks can be formed around the circular cavity under impact loads. Also, drastic spalling failure occurs at the top and bottom of the cavity (see Table 3) because of high concentrated compressive stresses. With the regard to the shear cracks appeared in the impact loading tests, its formation mechanism is the same as that under uniaxial compression; that is, the end friction effect leads to the appearance of the shear band. As the imposed load increases further, the shear band evolves into shear cracks and merges with the cavity eventually. Clearly, the dynamic failure behavior of the cavity under impact loads can be well explained based on the dynamic stress distribution on the periphery of the cavity.

With regard to the rock fragmentation characteristics, the greater the energy absorbed, the more easily the sample is broken. Therefore, it is easy to understand that the sample with large dissipated energy density tends to fail violently. If the size of rock fragmentation is small, the fractal dimension is

large according to fractal theory of rock. Besides, it is universally acknowledged that rock burst and spalling failure or V-notched failure in hard rock tunnel under high in situ stresses can be induced by blasting loads. Studies have shown that these disasters in deep rock engineering usually occur at the bottom/top or two sides of the tunnel [66–68], depending on the stress distribution. In this study, the spalling failure is found to happen where the dynamic concentrated compressive stress is greatest, i.e., the roof and floor of the circular cavity in the samples. Obviously, the laboratory findings are consistent with the actual engineering, which is beneficial to the prevention and control of rock disasters. Given that the cross-sectional shapes of the openings in rock engineering are mostly noncircular, such as horseshoe, rectangle, trapezoid, and inverted *U*-shape. Therefore, the dynamic failure response and stress distributions around these openings in rock samples under impact loads will be further studied in the next work. Also, considering the dual effects of the blasting dynamic load and geo-stress exerted on the tunnel, we will explore the failure behavior of rock samples with openings under static-dynamic coupled loads in the future. Moreover, the possible influencing factors such as lithology, discontinuities, loading methods, opening shape, number as well as their configuration will be taken into account.

5 Conclusions

In this paper, the dynamic mechanical response and energy dissipation of rock samples having a circular cavity of different sizes were deeply investigated via a modified SHPB test equipment. Based on the experimental and theoretical analysis results, the following points can be concluded:

- (1) The mechanical parameters of the rock sample having a cavity such as dynamic compressive strength, peak strain and brittleness index are greatly degraded by the cavity, and the weakening degree relies on the cavity radius.
- (2) Under dynamic loads, no tensile cracks as in uniaxial loading tests are formed, and spalling cracks occur first on the top and bottom of the cavity, followed by the shear cracks appearing on the diagonals. The intersection of the shear cracks with the cavity brings about the instability of the sample, with a shear failure mode. With the rise of the cavity radius, both the dissipated energy density and fractal dimension increases gradually. This indicates that the sample failure is more and more severe, and the rock fragments are getting smaller and smaller.
- (3) On the boundary of the circular cavity, the maximum compressive stress concentration factor is about 2.8 on the roof and floor, while the minimum value is close to zero on the sidewalls. The dynamic stress distribution

law can fully explain the fracture development around the cavity under impact loading.

Acknowledgments The authors are very grateful to Prof. Xibing Li, one of the pioneers in the field of rock dynamics, for affording excellent laboratory facilities for impact loading tests. His fruitful achievements and forward-looking academic ideas also provide strong support for this research.

Funding This study received the financial support from the National Natural Science Foundation of China (grant numbers: 51774321 and 51804163) and the China Postdoctoral Science Foundation (grant number: 2018M642678).

Declarations

Conflict of Interest The authors declare that they have no conflict of interest.

References

1. Lee H, Jeon S (2011) An experimental and numerical study of fracture coalescence in pre-cracked specimens under uniaxial compression. *Int J Solids Struct* 48(6):979–999. <https://doi.org/10.1016/j.ijsolstr.2010.12.001>
2. Saadat M, Taheri A (2019) A numerical approach to investigate the effects of rock texture on the damage and crack propagation of a pre-cracked granite. *Comput Geotech* 111:89–111. <https://doi.org/10.1016/j.compgeo.2019.03.009>
3. Cao RH, Cao P, Lin H, Pu CZ, Ou K (2016) Mechanical behavior of brittle rock-like specimens with pre-existing fissures under uniaxial loading: experimental studies and particle mechanics approach. *Rock Mech Rock Eng* 49(3):763–783. <https://doi.org/10.1007/s00603-015-0779-x>
4. Huang YH, Yang SQ (2019) Mechanical and cracking behavior of granite containing two coplanar flaws under conventional triaxial compression. *Int J Damag Mech* 28(4):590–610. <https://doi.org/10.1177/1056789518780214>
5. Bobet A (2000) The initiation of secondary cracks in compression. *Eng Fract Mech* 66(2):187–219. [https://doi.org/10.1016/S0013-7944\(00\)00009-6](https://doi.org/10.1016/S0013-7944(00)00009-6)
6. Bi J, Zhou XP, Qian QH (2016) The 3D numerical simulation for the propagation process of multiple pre-existing flaws in rock-like materials subjected to biaxial compressive loads. *Rock Mech Rock Eng* 49(5):1611–1627. <https://doi.org/10.1007/s00603-015-0867-y>
7. Jin J, Cao P, Chen Y, Pu CZ, Mao DW, Fan X (2017) Influence of single flaw on the failure process and energy mechanics of rock-like material. *Comput Geotech* 86:150–162. <https://doi.org/10.1016/j.compgeo.2017.01.011>
8. Bobet A, Einstein HH (1998) Fracture coalescence in rock-type materials under uniaxial and biaxial compression. *Int J Rock Mech Min* 35(7):863–888. [https://doi.org/10.1016/S0148-9062\(98\)00005-9](https://doi.org/10.1016/S0148-9062(98)00005-9)
9. Gao YH, Feng XT (2019) Study on damage evolution of intact and jointed marble subjected to cyclic true triaxial loading. *Eng Fract Mech* 215:224–234. <https://doi.org/10.1016/j.engfracmech.2019.05.011>
10. Yang SQ, Huang YH (2017) An experimental study on deformation and failure mechanical behavior of granite containing a single fissure under different confining pressures. *Environ Earth Sci* 76:364–385. <https://doi.org/10.1007/s12665-017-6696-4>

11. Aliha MRM, Ayatollahi MR, Smith DJ, Pavier MJ (2010) Geometry and size effects on fracture trajectory in a limestone rock under mixed mode loading. *Eng Fract Mech* 77(11):2200–2212. <https://doi.org/10.1016/j.engfracmech.2010.03.009>
12. Erarslan N, Williams DJ (2013) Mixed-mode fracturing of rocks under static and cyclic loading. *Rock Mech Rock Eng* 46(5):1035–1052. <https://doi.org/10.1007/s00603-012-0303-5>
13. Dang WG, Konietzky H, Herbst M, Frühwirt T (2020) Cyclic frictional responses of planar joints under cyclic normal load conditions: laboratory tests and numerical simulations. *Rock Mech Rock Eng* 53:337–364. <https://doi.org/10.1007/s00603-019-01910-9>
14. Dang WG, Konietzky H, Li X (2019) Frictional responses of concrete-to-concrete bedding planes under complex loading conditions. *Geomech Eng* 17(3):253–259. <https://doi.org/10.12989/gae.2019.17.3.253>
15. Li XB, Zhou T, Li DY (2017) Dynamic strength and fracturing behavior of single-flawed prismatic marble specimens under impact loading with a split-Hopkinson pressure bar. *Rock Mech Rock Eng* 50(1):29–44. <https://doi.org/10.1007/s00603-016-1093-y>
16. Bahaaddini M, Sharrock G, Hebblewhite BK (2013) Numerical investigation of the effect of joint geometrical parameters on the mechanical properties of a non-persistent jointed rock mass under uniaxial compression. *Comput Geotech* 49:206–225. <https://doi.org/10.1016/j.compgeo.2012.10.012>
17. Wong LNY, Li HQ (2013) Numerical study on coalescence of two pre-existing coplanar flaws in rock. *Int J Solids Struct* 50(22–23):3685–3706. <https://doi.org/10.1016/j.ijsolstr.2013.07.010>
18. Zhao YL, Zhang LY, Wang WJ, Pu CZ, Wan W, Tang JZ (2016) Cracking and stress-strain behavior of rock-like material containing two flaws under uniaxial compression. *Rock Mech Rock Eng* 49(7):2665–2687. <https://doi.org/10.1007/s00603-016-0932-1>
19. Feng P, Dai F, Liu Y, Xu NW, Fan PX (2018) Effects of coupled static and dynamic strain rates on mechanical behaviors of rock-like specimens containing pre-existing fissures under uniaxial compression. *Can Geotech J* 55(5):640–652. <https://doi.org/10.1139/cgj-2017-0286>
20. Li DY, Han ZY, Sun XL, Zhou T, Li XB (2019) Dynamic mechanical properties and fracturing behavior of marble specimens containing single and double flaws in SHPB tests. *Rock Mech Rock Eng* 52:1623–1643. <https://doi.org/10.1007/s00603-018-1652-5>
21. Haeri H, Khaloo A, Marji MF (2015) Experimental and numerical analysis of Brazilian discs with multiple parallel cracks. *Arab J Geosci* 8(8):5897–5908. <https://doi.org/10.1007/s12517-014-1598-1>
22. Germanovich LN, Salganik RL, Dyskin AV, Lee KK (1994) Mechanisms of brittle fracture of rock with pre-existing cracks in compression. *Pure Appl Geophys* 143(1–3):117–149. <https://doi.org/10.1007/BF00874326>
23. Dyskin AV, Sahouryeh E, Jewell RJ, Joer H, Ustinov KB (2003) Influence of shape and locations of initial 3-D cracks on their growth in uniaxial compression. *Eng Fract Mech* 70(15):2115–2136. [https://doi.org/10.1016/S0013-7944\(02\)00240-0](https://doi.org/10.1016/S0013-7944(02)00240-0)
24. Zhang ZN, Wang DY, Zheng H, Ge XR (2012) Interactions of 3D embedded parallel vertically inclined cracks subjected to uniaxial compression. *Theor Appl Fract Mech* 61:1–11. <https://doi.org/10.1016/j.tafmec.2012.08.001>
25. Mondal S, Olsen-Kettle L, Gross L (2019) Simulating damage evolution and fracture propagation in sandstone containing a preexisting 3-D surface flaw under uniaxial compression. *Int J Numer Anal Met* 43(7):1448–1466. <https://doi.org/10.1002/nag.2908>
26. Zhou T, Zhu JB, Ju Y, Xie HP (2019) Volumetric fracturing behavior of 3D printed artificial rocks containing single and double 3D internal flaws under static uniaxial compression. *Eng Fract Mech* 205:190–204. <https://doi.org/10.1016/j.engfracmech.2018.11.030>
27. Zhou T, Zhu JB, Xie HP (2020) Mechanical and volumetric fracturing behaviour of three-dimensional printing rock-like samples under dynamic loading. *Rock Mech Rock Eng* 53:2855–2864. <https://doi.org/10.1007/s00603-020-02084-5>
28. Hoek E (1965) Rock fracture under static stress conditions. University of Cape Town, Cape Town, South Africa
29. Wong RHC, Lin P, Tang CA (2006) Experimental and numerical study on splitting failure of brittle solids containing single pore under uniaxial compression. *Mech Mater* 38(1–2):142–159. <https://doi.org/10.1016/j.mechmat.2005.05.017>
30. Sammis CG, Ashby MF (1986) The failure of brittle porous solids under compressive stress states. *Acta Metall Sin* 34(3):511–526. [https://doi.org/10.1016/0001-6160\(86\)90087-8](https://doi.org/10.1016/0001-6160(86)90087-8)
31. Zhao XD, Zhang HX, Zhu WC (2014) Fracture evolution around pre-existing cylindrical cavities in brittle rocks under uniaxial compression. *Trans Nonferrous Metals Soc* 24(3):806–815. [https://doi.org/10.1016/S1003-6326\(14\)63129-0](https://doi.org/10.1016/S1003-6326(14)63129-0)
32. Carter BJ, Lajtai EZ, Petukhov A (1991) Primary and remote fracture around underground cavities. *Int J Numer Anal Met* 15(1):21–40. <https://doi.org/10.1002/nag.1610150103>
33. Zeng W, Yang SQ, Tian WL (2018) Experimental and numerical investigation of brittle sandstone specimens containing different shapes of holes under uniaxial compression. *Eng Fract Mech* 200:430–450. <https://doi.org/10.1016/j.engfracmech.2018.08.016>
34. Wu H, Zhao GY, Liang WZ (2020) Mechanical properties and fracture characteristics of pre-holed rocks subjected to uniaxial loading: a comparative analysis of five hole shapes. *Theor Appl Fract Mec* 105:102433. <https://doi.org/10.1016/j.tafmec.2019.102433>
35. Fakhimi A, Carvalho F, Ishida T, Labuz JF (2002) Simulation of failure around a circular opening in rock. *Int J Rock Mech Min Sci* 39:507–515. [https://doi.org/10.1016/S1365-1609\(02\)00041-2](https://doi.org/10.1016/S1365-1609(02)00041-2)
36. Zhang SR, Sun B, Wang C, Yan L (2014) Influence of intermediate principal stress on failure mechanism of hard rock with a pre-existing circular opening. *J Cent South Univ* 21:1571–1582. <https://doi.org/10.1007/s11771-014-2098-x>
37. Wang SY, Sloan SW, Tang CA (2013) Three-dimensional numerical investigations of the failure mechanism of a rock disc with a central or eccentric hole. *Rock Mech Rock Eng* 47(6):2117–2137. <https://doi.org/10.1007/s00603-013-0512-6>
38. Zhao ZL, Jing HW, Shi XS, Han GS (2019) Experimental and numerical study on mechanical and fracture behavior of rock-like specimens containing pre-existing holes flaws. *Eur J Environ Civ Eng* 1–21. <https://doi.org/10.1080/19648189.2019.1657961>
39. Yang SQ, Huang YH, Tan WL, Zhu JB (2017) An experimental investigation on strength, deformation and crack evolution behavior of sandstone containing two oval flaws under uniaxial compression. *Eng Geol* 217:35–48. <https://doi.org/10.1016/j.enggeo.2016.12.004>
40. Zhou ZL, Tan LH, Cao WZ, Zhou ZY, Cai X (2017) Fracture evolution and failure behaviour of marble specimens containing rectangular cavities under uniaxial loading. *Eng Fract Mech* 184:183–201. <https://doi.org/10.1016/j.engfracmech.2017.08.029>
41. Wu H, Zhao GY, Liang WZ (2019) Mechanical response and fracture behavior of brittle rocks containing two inverted U-shaped holes under uniaxial loading. *Appl Sci* 9(24):5327. <https://doi.org/10.3390/app9245327>
42. Lin P, Wong RHC, Tang CA (2015) Experimental study of coalescence mechanisms and failure under uniaxial compression of granite containing multiple holes. *Int J Rock Mech Min Sci* 77:313–327. <https://doi.org/10.1016/j.ijrmm.2015.04.017>
43. Huang YH, Yang SQ, Ranjith PG, Zhao J (2017) Strength failure behavior and crack evolution mechanism of granite containing pre-existing non-coplanar holes: experimental study and particle flow modeling. *Comput Geotech* 88:182–198. <https://doi.org/10.1016/j.compgeo.2017.03.015>

44. Huang YH, Yang SQ, Tian WL (2019) Cracking process of a granite specimen that contains multiple pre-existing holes under uniaxial compression. *Fatigue Fract Eng Mater Struct* 42:1341–1356. <https://doi.org/10.1111/ffe.12990>
45. Jespersen C, Maclaughlin M, Hudyma N (2010) Strength, deformation modulus and failure modes of cubic analog specimens representing macroporous rock. *Int J Rock Mech Min Sci* 47(8):1349–1356. <https://doi.org/10.1016/j.ijmms.2010.08.015>
46. Haeri H, Khaloo A, Marji MF (2015) Fracture analyses of different pre-holed concrete specimens under compression. *Acta Mech Sinica* 31:855–870. <https://doi.org/10.1007/s10409-015-0436-3>
47. Wang SY, Sloan SW, Sheng DC, Tang CA (2012) Numerical analysis of the failure process around a circular opening in rock. *Comput Geotech* 39:8–16. <https://doi.org/10.1016/j.compgeo.2011.08.004>
48. Spetz A, Denzer R, Tudisco E, Dahlblom O (2020) Phase-field fracture modelling of crack nucleation and propagation in porous rock. *Int J Fract* 224:31–46. <https://doi.org/10.1007/s10704-020-00444-4>
49. Yin Q, Jing HW, Ma GW (2015) Experimental study on mechanical properties of sandstone specimens containing a single hole after high-temperature exposure. *Géotech Lett* 5(1):43–48. <https://doi.org/10.1680/geolett.14.00121>
50. Qiu JD, Li XB, Li DY, Zhao YZ, Hu CW, Liang LS (2020) Physical model test on the deformation behavior of an underground tunnel under blasting disturbance. *Rock Mech Rock Eng*. <https://doi.org/10.1007/s00603-020-02249-2>
51. Zhou Z, Cai X, Li X, Cao WZ, Du XM (2020) Dynamic response and energy evolution of sandstone under coupled static–dynamic compression: insights from experimental study into deep rock engineering applications. *Rock Mech Rock Eng* 53(3):1305–1331. <https://doi.org/10.1007/s00603-019-01980-9>
52. Qiu JD, Li DY, Li XB, Zhu QQ (2020) Numerical investigation on the stress evolution and failure behavior for deep roadway under blasting disturbance. *Soil Dyna Earthq Eng* 137:106278. <https://doi.org/10.1016/j.soildyn.2020.106278>
53. Xia KW, Yao W (2015) Dynamic rock tests using split Hopkinson (Kolsky) bar system – a review. *J Rock Mech Geotech Eng* 7(1):27–59. <https://doi.org/10.1016/j.jrmge.2014.07.008>
54. Dai F, Huang S, Xia KW, Tan ZY (2010) Some fundamental issues in dynamic compression and tension tests of rocks using split Hopkinson pressure bar. *Rock Mech Rock Eng* 43:657–666. <https://doi.org/10.1007/s00603-010-0091-8>
55. Zhang QB, Zhao J (2014) A review of dynamic experimental techniques and mechanical behaviour of rock materials. *Rock Mech Rock Eng* 47:1411–1477. <https://doi.org/10.1007/s00603-013-0463-y>
56. Luo Y, Gong FQ, Liu DQ, Wang SY, Si XF (2019) Experimental simulation analysis of the process and failure characteristics of spalling in D-shaped tunnels under true-triaxial loading conditions. *Tunn Undergr Sp Tech* 90:42–61. <https://doi.org/10.1007/s00603-013-0463-y>
57. Cai X, Zhou ZL, Du XM (2020) Water-induced variations in dynamic behavior and failure characteristics of sandstone subjected to simulated geo-stress. *Int J Rock Mech Min Sci* 130:104339–104748. <https://doi.org/10.1016/j.ijmms.2007.08.013>
58. Li XB (2014) *Rock dynamics fundamentals and applications*. Science Press, Beijing
59. Han ZY, Li DY, Zhou T, Zhu QQ, Ranjith PG (2020) Experimental study of stress wave propagation and energy characteristics across rock specimens containing cemented mortar joint with various thicknesses. *Int J Rock Mech Min Sci* 131:104352. <https://doi.org/10.1016/j.ijmms.2020.104352>
60. Cai X, Zhou ZL, Zang HZ, Song ZY (2020) Water saturation effects on dynamic behavior and microstructure damage of sandstone: phenomena and mechanisms. *Eng Geol* 276:105760. <https://doi.org/10.1016/j.enggeo.2020.105760>
61. Li XB, Zhou T, Li DY, Wang ZW (2016) Experimental and numerical investigations on feasibility and validity of prismatic rock specimen in SHPB. *Shock Vib* 2016:7198980–7198913. <https://doi.org/10.1155/2016/7198980>
62. Wu H, Kulatilake PHSW, Zhao GY, Liang WZ, Wang EJ (2019) A comprehensive study of fracture evolution of brittle rock containing an inverted U-shaped cavity under uniaxial compression. *Comput Geotech* 116:103219. <https://doi.org/10.1016/j.compgeo.2019.103219>
63. Perfect E (1997) Fractal models for the fragmentation of rocks and soils: a review. *Eng Geol* 48(3–4):185–198. [https://doi.org/10.1016/S0013-7952\(97\)00040-9](https://doi.org/10.1016/S0013-7952(97)00040-9)
64. Wu H, Zhao GY, Liang WZ (2019) Investigation of cracking behaviour and mechanism of sandstone specimens with a hole under compression. *Int J Mech Sci* 163:105084. <https://doi.org/10.1016/j.ijmms.2019.105084>
65. Tao M, Ma A, Cao WZ, Li XB, Gong FQ (2017) Dynamic response of pre-stressed rock with a circular cavity subject to transient loading. *Int J Rock Mech Min Sci* 99:1–8. <https://doi.org/10.1016/j.ijmms.2017.09.003>
66. Feng F, Chen SJ, Li DY, Hu ST, Huang WP, Li B (2019) Analysis of fractures of a hard rock specimen via unloading of central hole with different sectional shapes. *Energy Sci Eng* 7(6):2265–2286. <https://doi.org/10.1002/ese3.432>
67. Zhu WC, Li ZH, Zhu L, Tang CA (2010) Numerical simulation on rockburst of underground opening triggered by dynamic disturbance. *Tunn Undergr Sp Tech* 25(5):587–599. <https://doi.org/10.1016/j.tust.2010.04.004>
68. Li XB, Gong FQ, Tao M, Dong LJ, Du K, Ma CD, Zhou ZL, Yin TB (2017) Failure mechanism and coupled static–dynamic loading theory in deep hard rock mining: a review. *J Rock Mech Geotech Eng* 9(4):767–782. <https://doi.org/10.1016/j.jrmge.2017.04.004>

Publisher's Note Springer Nature remains neutral with regard to jurisdictional claims in published maps and institutional affiliations.